

2.3. X-ray Imaging and Microfocusing

The thrust of the x-ray imaging and microfocusing program in SRI CAT is to develop state-of-the-art x-ray focusing optics and techniques, and to apply them to outstanding problems in the materials, environmental, biological, and biomedical fields. Our effort in these areas is roughly evenly split between development of novel microfocusing and imaging optics, instrumentation, and techniques with unprecedented capabilities that capitalize on the high brilliance of APS sources, and their application to problems that are either less efficiently studied or simply cannot be addressed by other means. The most mature and heavily subscribed of these instruments are the hard and soft *x-ray scanning microprobes*, which enable imaging and spectroscopic study of samples at high spatial resolution, currently down to 150 nm at 8 keV and 60 nm at 2 keV, using absorption and fluorescence contrast mechanisms. The hard x-ray scanning microprobe was one of three Argonne projects that won the Year 2000 R&D 100 Award sponsored by *R&D Magazine*. It was developed by B. Lai, Z. Cai, J. Maser, P. Ilinski, D. Legnini, and W. Yun. The newest such instrument operating in SRI CAT is the x-ray fluorescence microprobe located in the 2-ID-E experimental station. Zone-plate lenses are the key optical elements used to form the tightly focused x-ray microprobes in these instruments. Improving both the x-ray focusing resolution and efficiency of zone plates is a central goal of the SRI-CAT imaging program. In particular, *stacked zone plates* offer a practical means to realize both high efficiency and high resolution, most

notably for high-energy x-rays. The scanning microprobes are primarily used for two-dimensional (2D) imaging. Other 2D imaging methods, including interferometric and noninterferometric *phase contrast imaging*, are also being developed as part of this program. *High-throughput tomography*, on the other hand, offers fully three-dimensional (3D) imaging on time scales of minutes down to the 1 μm spatial resolution scale. The raw speed of this method makes possible the dynamic study of nonstatic samples as they evolve in 3D or enables study of a large number of samples in 3D.

2.3.1 A New Facility: the 2-ID-E X-ray Fluorescence Microprobe

Sector 2 at the APS is dedicated to microbeam applications using zone-plate optics. Zone plates take advantage of the high brilliance of third-generation light sources by using the spatially coherent fraction of the beam and focusing it into a diffraction-limited spot of suboptical dimensions. When using zone plates to achieve highest x-ray optical resolution, only a small part of a typical undulator beam can be used. By dividing the wavefront of the beam, several x-ray microprobes can be operated in parallel at a small cost in flux density, spatial resolution and flexibility. Parallelizing of operation is particularly useful for elemental mapping using x-ray fluorescence, where small data rates limit the number of experiments that can be performed in a reasonable amount of time.

2.3.1.1 2-ID-E side-branch beamline

To make use of additional coherent modes in the undulator beam, we have developed a side-branch beamline with a dedicated x-ray

fluorescence microprobe in the 2-ID-E experimental station. This branch line is operated in parallel to the 2-ID-D end station. To divide the wavefront of the undulator, a beam-splitting crystal is positioned 0.3 mm from the center of the beam at a distance of 62 m from the source. The crystal deflects the outboard part of the undulator beam into the branch station, while letting the center of the beam pass through to the 2-ID-D end station. The flux density of the deflected beam is 15% - 20% less than in the beam center, thus providing quite reasonable conditions for micro-fluorescence studies.

2.3.1.2 Optimized design

Since the 2-ID-E microprobe is designed to operate only in x-ray fluorescence mode, significant optimization of the design could be achieved. A three-element low-energy germanium (LEGe) detector with a resolution of 150 eV collects the fluorescence spectra. Two zone plates with different x-ray optical resolution are mounted next to each other and can be changed at the push of a button. This allows a change of magnification and resolution similar to a change of objective lenses in an optical microscope and gives the user a choice between operation at highest resolution (0.25 μm) or an order-of-magnitude increase in photon flux at lower resolution. The specimen is mounted on a standardized kinematic mount in a chamber of leaded acrylic. This specimen chamber both serves to shield against the x-ray background in the 2-ID-E hutch and provides a gas-tight environment. During data acquisition, the specimen chamber is flooded with helium to both minimize Ar fluorescence from air and reduce absorption

of the fluorescence of low-Z elements. Kinematic specimen holders allow fast and precise mounting. Using an adaptor, the specimen holder can be mounted kinematically on a state-of-the-art optical microscope, allowing survey of the specimen prior to x-ray mapping, as well as accurate prealignment with respect to the x-ray beam. This is invaluable when pre-positioning thin specimens with little x-ray absorption, such as cells and thin films. Significant attention has been paid recently to developing an intuitive user interface. This screen includes "in/out" buttons for exchange of x-ray optics and specimen, and a first version of tools that align the x-ray optics of the microprobe automatically at the push of a button. Users from fields like medical sciences, biology or environmental materials sciences, who are typically not familiar with the operation of complex synchrotron instrumentation, are able to operate independently after only a few hours of training.

2.3.1.3 Performance

With closed white-beam slits and optimized undulator gap, the 2-ID-E microprobe operates with a spatial resolution of 0.5 μm \times 0.25 μm and focused flux of 10^8 ph/s (see Fig. 2.5). Opening the white-beam slits increases the spot size to 1.2 μm \times 0.3 μm and yields a focused flux of 10^9 ph/s. Using the second zone plate, with a focal length of 40 cm and an outermost zone width of 250 nm, a focused flux of 2×10^{10} ph/s is obtained with open white-beam slits.

We have begun to build a user program in both biomedical and materials sciences. Experiments performed in the first six months of operation include mapping of the

trace metal distribution in eukaryotic cells and tissues, study of metals distributions in different organisms in the marine food chain (from copepods to bacteria), study of plants, both wild-type and genetically engineered, the study of trace element distributions in optical fibers, and characterization of the composition of Zr alloys in cladding for nuclear fuel rods.

Significant effort has been invested in different instrumentation issues, in particular, the characterization of and use of near-field stacking of zone plates, which significantly increases the diffraction efficiency, and commissioning of a multi-element detector. Significant progress has also been made in efficiently collecting full fluorescence spectra for each image pixel and using principal component analysis for data analysis.

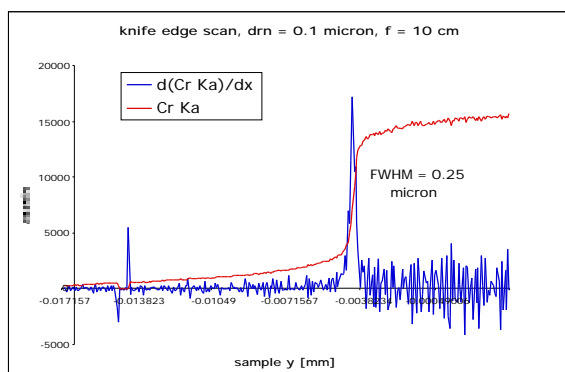


Fig. 2.5. Resolution measurement using a Cr knife-edge. X-ray fluorescence of the knife-edge is collected using an energy-dispersive LGe detector. Fitting of the data with an error function and derivation of the measured curve yield a resolution of 0.25 μm .

2.3.2 A High-Throughput X-ray Microtomography System

2.3.2.1 System architecture

A third-generation synchrotron radiation source provides enough brilliance to acquire complete tomographic data sets at 100 nm or better resolution in a few minutes. To take advantage of such high-brilliance sources at the APS, we have constructed a pipelined data acquisition and analysis system (Fig. 2.6) in collaboration with the Argonne Mathematics and Computer Science Division (MCS). The system combines a fast detector, high-speed data networks, and massively parallel computers to rapidly acquire the projection data then remotely perform the preprocessing, reconstruction, and rendering calculations (Wang et al., 1999).

2.3.2.2 Data acquisition system

The high-throughput tomography data acquisition system is based at the 2-BM beamline. It uses a straight-ray projection imaging scheme and monochromatic x-rays of energies between 5 and 20 keV to produce an absorption contrast image on a scintillator screen. A visible-light objective lens and charge-coupled device (CCD) camera acquire the visible light image produced on the scintillator screen for each angular orientation of the sample as it is rotated about the vertical axis. Typically with our system configuration, we acquire 1024×1024 pixels projection every $0.25 - 0.50^\circ$ of sample rotation, producing up to 720 projections. Once the data set is available, a software preprocessing algorithm normalizes the data using whitefield images (sample removed from

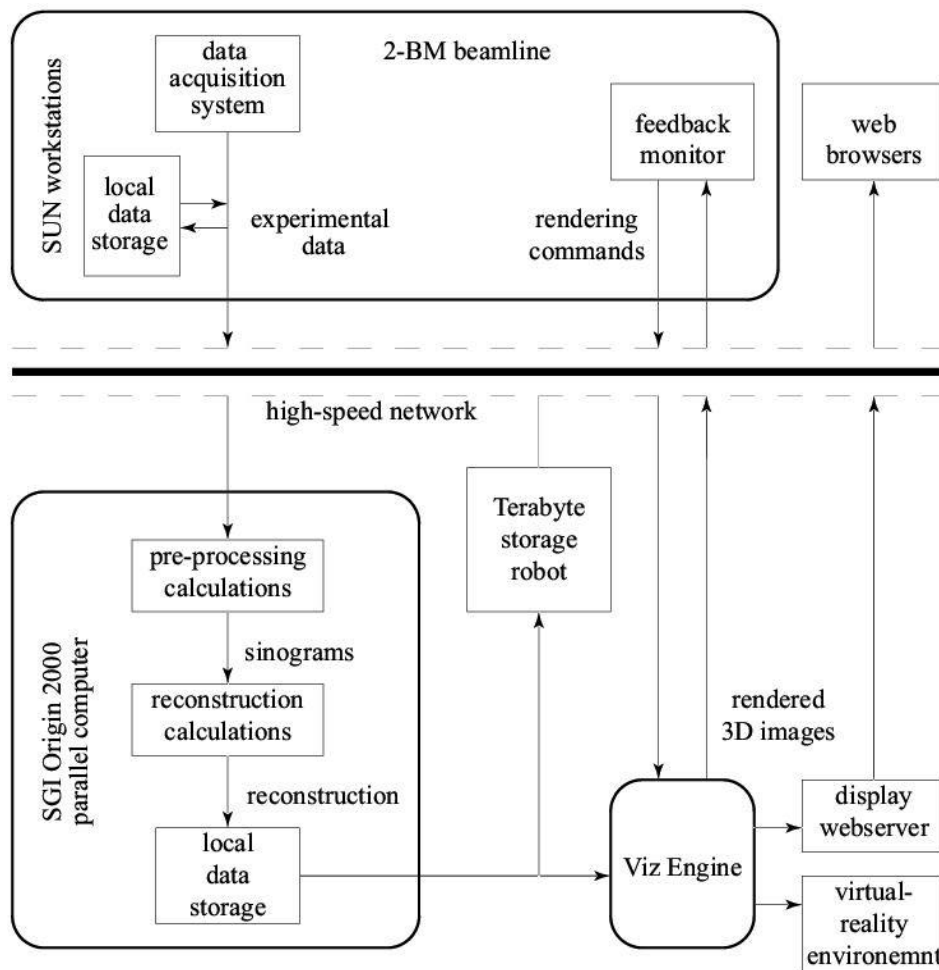


Fig. 2.6. Illustration of the data acquisition and computation pipeline. An operator at the experiment station in the APS controls the data acquisition system on a Sun workstation and views the reconstruction result on the feedback monitor. The data acquired at the beamline are first written to a local hard disk and then transferred via a 100 Mb/s network to the Mathematics and Computer Science Division. There the preprocessing and reconstruction calculations are performed by the parallel computer. The reconstruction results are saved to a hard disk then loaded into the Viz Engine. The Viz Engine provides rendered images interactively to the beamline feedback monitor via the high-speed network and also periodically writes rendered still images to a web server.

beam) and blackfield images (background with beam off), as well as aligns all the projections to a common rotation axis.

The user has a choice of two Princeton Instruments CCD cameras, depending on the exposure times and readout rate required. One camera uses a 1317×1025 pixel Kodak

CCD ($6.8 \mu\text{m}$ square pixels), thermoelectrically cooled to -15°C and driven by a ST-133 controller with 12 bits/pixel at 1 MHz. The other is a 1024×1024 pixel-thinned backside-illuminated SITE CCD ($24 \mu\text{m}$ square pixels), cooled by liquid nitrogen to -100°C and driven by a ST-138 controller with 16 bits/pixel at 240 KHz. The latter

camera is the more sensitive but slower of the two.

For scintillator screens we use either a CdWO_4 crystal or a YAG crystal with a 5- μm -thick Ce doped active layer. The CdWO_4 screen delivers a resolution of $\sim 3\ \mu\text{m}$ using a 5X objective lens with $\text{NA} = 0.1$ with the Kodak CCD. The resolution of the YAG screen is higher, depending on the objective lens and CCD camera used. Using the YAG screen, SITE CCD, and various objectives from 4X to 40X in magnification, we achieved a resolution of 0.8 to 6 μm and sample image field size of 0.6 to 6 mm. The efficiency of the CdWO_4 screen is about four times that of the YAG screen.

2.3.2.3 Control software

All functions performed during a tomography experiment are automatically controlled by an interactive data language (IDL) language graphical user interface and script that uses Experimental Physics and Industrial Control System (EPICS) channel access routines to move motors and actuate the shutter, as well as to page the user when the data set is completed. Another important task performed by the IDL script is to log all the experimentally relevant information into a file as part of the data set. The projection data is stored in the data set (one file per projection) in the highly portable hierarchical data format (HDF) created by the National Center for Supercomputing Applications.

2.3.2.4 Performance

Using this system, complete tomographic data sets can be obtained in tens of minutes to hours depending on the resolution and

contrast desired. Immediately after each image in the data set is acquired, it is transferred to a massively parallel supercomputer (Silicon Graphics Inc. Origin 2000 with 128 nodes) at the MCS building for normalization, filtering, and alignment calculations. The aligned projection images are then assembled into sinogram format for reconstruction calculations. Using 80 nodes, a data set containing 720 projections, each with 1024×1024 pixels, takes about 17 minutes to reconstruct with the filtered back-projection method. A smaller data set with 360 projections with 512×512 pixels takes less than 1 minute. When the reconstruction calculations are complete, a visualization computer loads the results and performs rendering calculations in hardware, makes rendered images available to the beamline users, and allows the users to manipulate the rendering interactively. This system is capable of examining a large number of samples at submicrometer 3D resolution or studying the full 3D structure of a dynamically evolving sample on a 10 minute temporal scale. Test results obtained with the instrument, showing 3D images of a cricket's head, are shown in Figs. 2.7 and 2.8.

We are currently improving on two limitations of the system: a new broadband multilayer monochromator will be used for fast tomography instead of the double-crystal monochromator currently in use, which has an unnecessarily narrow energy bandwidth, and a new CCD camera with a 10 frame/s transfer rate is under test to use in place of the slower cameras. These two improvements should increase the time resolution to the 1 min scale. A full-field imaging-type x-ray microscope using zone plate optics is currently being developed at

the 2-ID-B beamline and has demonstrated 100 nm spatial resolution. We plan to integrate this microscope with the high-throughput reconstruction infrastructure to perform high-throughput *nanotomography*.

2.3.2.5 Local parallel processing

One of the major problems to be solved when dealing with high-throughput tomography data is the scale and complexity

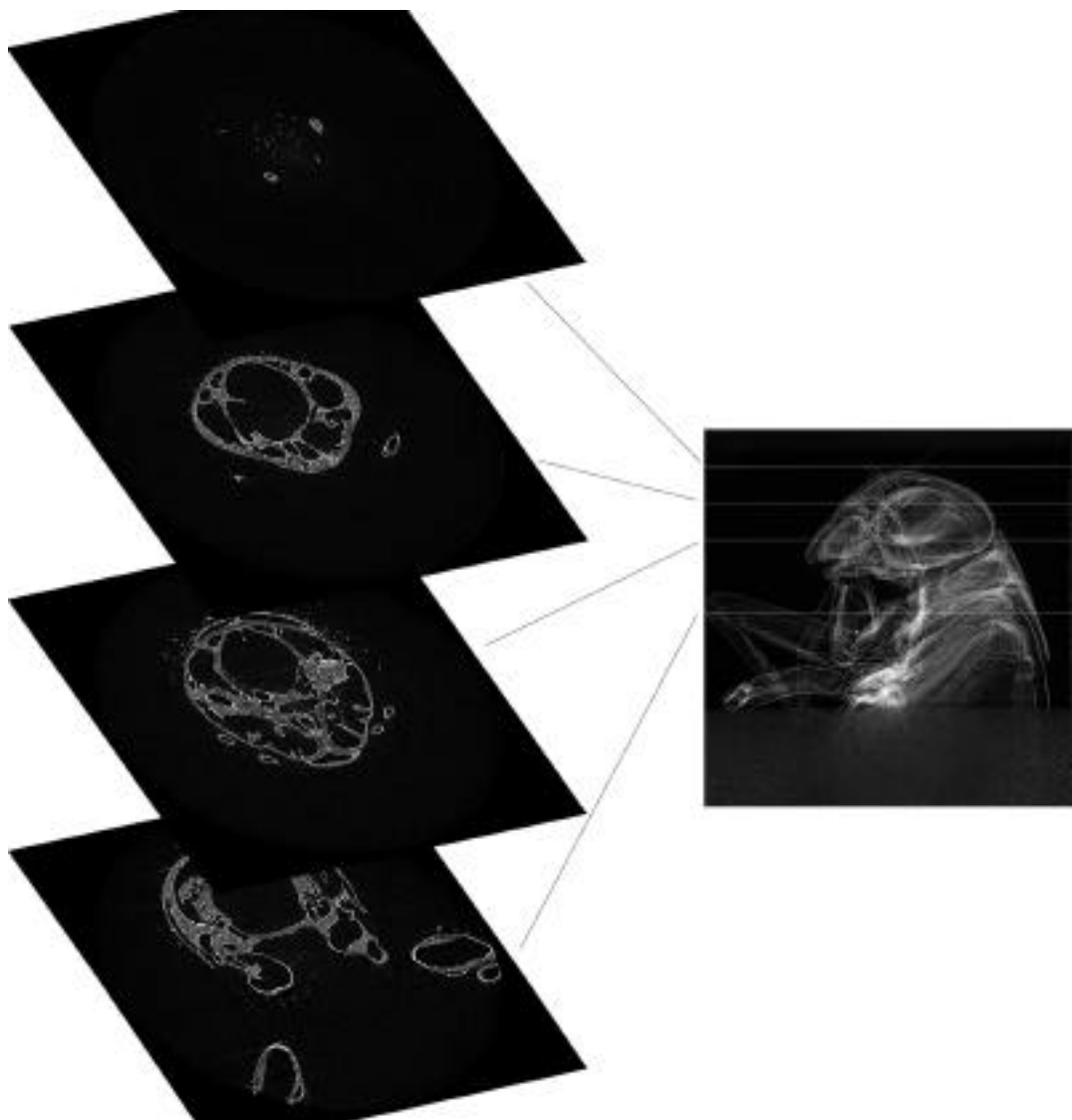


Fig. 2.7. Reconstructed sections from the cricket data. Four sections of the reconstruction volume as indicated on the projection image are shown. The fine features, such as individual hair and details in the skeletal structure including small cracks, are clearly visible.

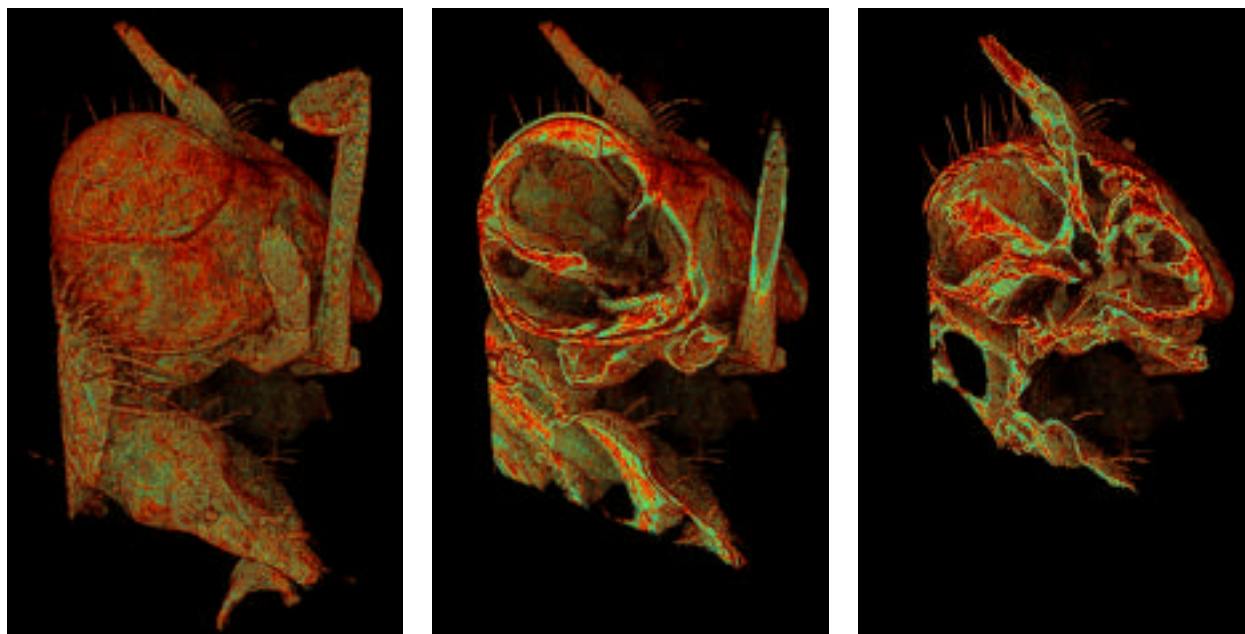


Fig. 2.8. Three rendered images from the cricket reconstruction, digitally cut at different planes to show the internal structures of the cricket's head.

of the data analysis, which requires rapid preprocessing, sinogram generation, 3D reconstruction, and visualization. In addition to supercomputer-based data analysis, we have developed a new method that uses the Message Passing Interface (MPI) software standard to combine multiple PC-class computers into a powerful yet locally available parallel computing system. Among the advantages of this approach are its accessibility, portability, ease of use, and relatively low cost.

MPI system

MPI is a library specification for message passing designed for both massively parallel machines and workstation clusters widely available, with free and vendor-supplied implementations. Key benefits of employing the MPI standard are its ease of use and wide portability (it runs under Unix

including AIX, Digital Unix, FreeBSD, HP-UX, IRIX, LINUX, Solaris, and SunOS, as well as Windows 95/NT and MAC OS).

We used MPICH for our implementation of the MPI standard. MPICH is a freely available, portable implementation of the Message-Passing Interface Standard developed by the Argonne Mathematics and Computer Science Division for Windows NT and other operating systems. It was chosen to implement a client-server model for performing reconstructions. In this model, a single process acts as a server to hand out jobs to many clients running on individual Windows NT workstations on the network (Fig. 2.9).

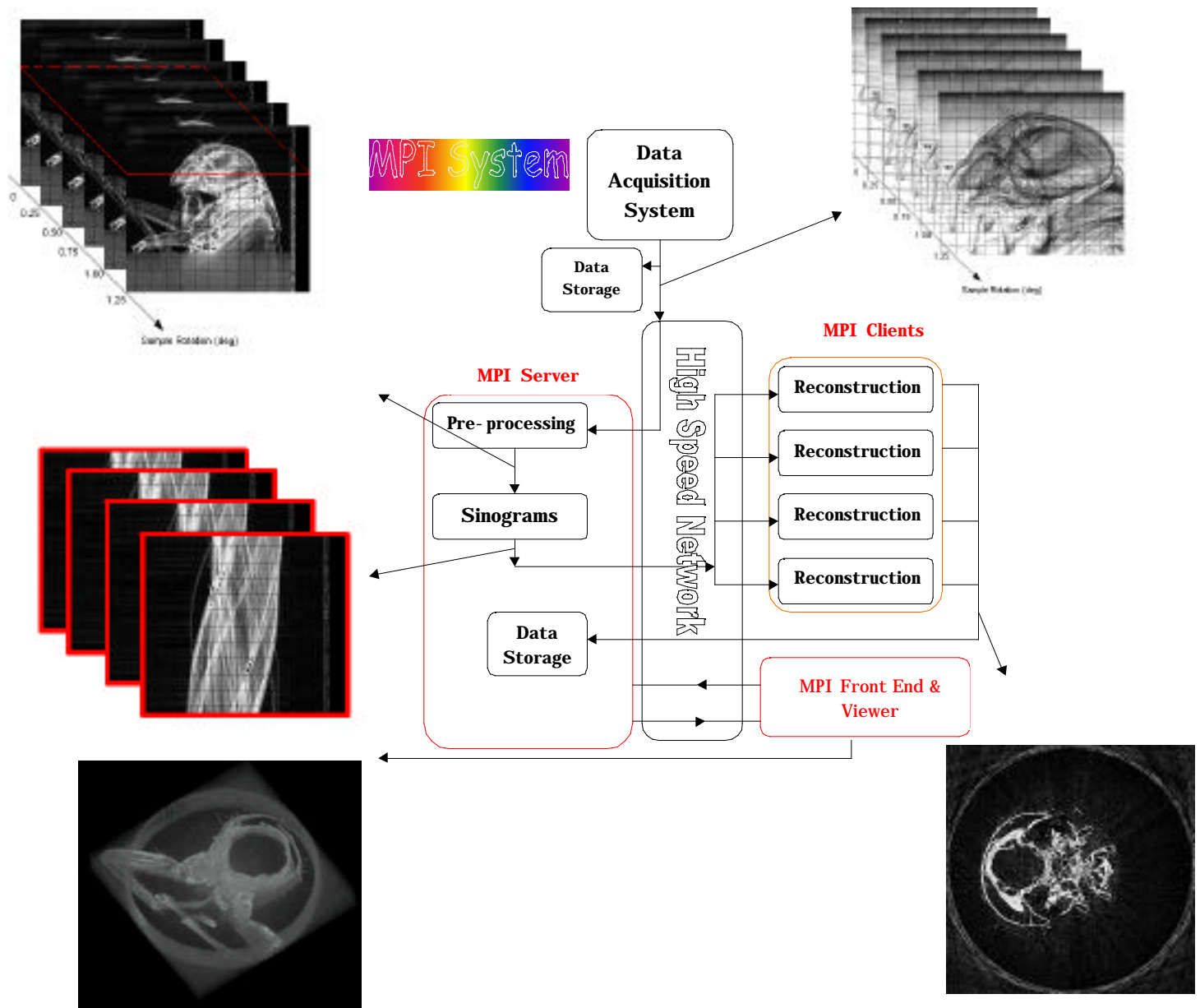


Fig. 2.9. The MPI client/server system used for tomography reconstruction.

The clients are typically the calculation engines of the system and perform a simple loop of operations: request a new sinogram, perform the reconstruction of the sinogram, send the server the completed reconstruction, then request a new sinogram. The clients perform these tasks in parallel to one another, since each client is typically running on its own processor.

The server's job is to respond to requests from the various clients and coordinate the flow of data from the disk system over the network and back to disk. The server first creates a number of sinograms from the

preprocessed files on disk. Once this is done, it waits for individual clients to make requests. The sinograms are handed out on a first-request, first-served basis to the clients. The server also performs the task of collecting the completed reconstruction and writing it to disk.

A specialized client has also been written to serve as a front end to the system. The front end makes requests of the server to alter various system parameters or to get information to display to the user about the current state of the system.

A simple configuration file allows the user a way to start up the entire system from a single machine. This configuration file dictates which processors on the network will be used as the server, the front end, or the many clients. This client/server approach to parallelize time-consuming calculations was straightforward to implement and can be readily applied to a wider range of calculation intensive problems. To view tomography data, we developed a simple viewer that recovers all the experimentally relevant information from the tomography data set and allows the user to easily browse the raw data, as well as normalized data, sinograms, and reconstructed slices.

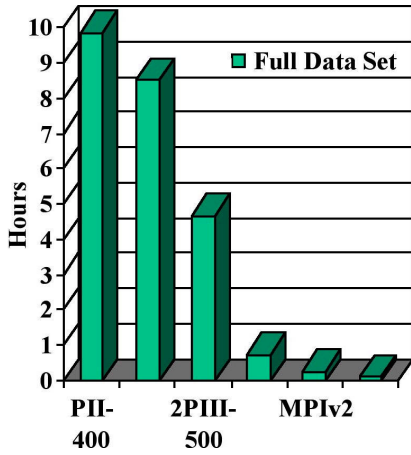


Fig. 2.10. Total reconstruction time (h) for a 360 projection set of 512x512 pixel projections. MPIv3 completes a reconstruction of the full data set in 7 min.

System performance

A first demonstration of the MPI system shows that the reconstruction time reduces proportionally with the number of processors used. At this stage, the network and disk data transport do not yet limit the calculation speed, although we expect this to

be the main limitation for a system with 20 or more processors. The results are shown in Figs. 2.10 and 2.11. Setup of a larger NT cluster (>20 PCs) is ongoing. We anticipate that these developments will provide the user with a powerful analysis tool for high-throughput tomography experiments.

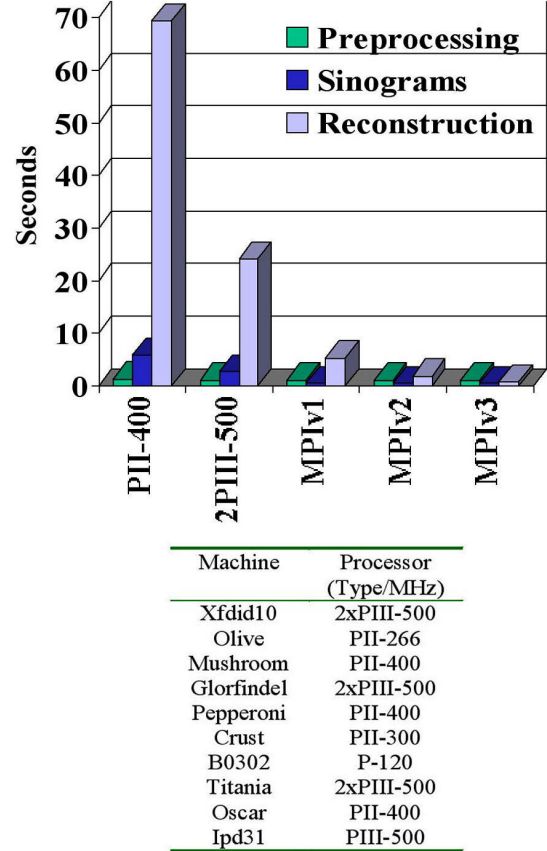


Fig. 2.11. Average reconstruction time (s) per 512x512 pixel slice. For the MPI cluster defined in the table (bottom), we obtained an almost linear reduction of the time to reconstruct a single slice. MPIv1-2-3 refers to a progression of three system upgrades. MPIv3 shows an average of 0.7 s/slice.

2.3.3 Stacked Zone Plates

2.3.3.1 Near-field stacking of zone plates

We use Fresnel zone plates as focusing and imaging elements in hard x-ray microprobes at photon energies typically between 6 and 30 keV. While zone plates have allowed us to push the spatial resolution of hard x-ray microprobes towards the 0.1 μm region, highest resolution can currently be obtained only at reduced diffraction efficiency due to manufacturing limitations with respect to the aspect ratios of zone plates. To increase the effective thickness of zone plates, we have begun to stack several identical zone plates on-axis in close proximity. If the zone plates are aligned laterally to within better than one outermost zone width and longitudinally within optical near-field, they form a single optical element of larger effective thickness and improved efficiency and signal/noise ratio. This allows us both to use zone plates of moderate outermost zone width in the hard x-ray range and to increase the efficiency of zone plates with small outermost zone widths for the multi-keV range.

For lateral alignment dr_n of two zone plates, we require the typical accuracy $\text{dr}_n < 1/3 \text{ dr}_n$, where dr_n is the outermost zone width. To quantify the required proximity p between two zone plates, we request that both zone plates are aligned to within optical near-field. For two zone plates with outermost zone width dr_n , the near-field condition can be written as $p < \text{dr}_n^2 / \lambda$. To match the above condition for the lateral alignment dr_n , we require that $p < 1/3 \text{ dr}_n^2 / \lambda$ for the proximity between two zone plates. Table 2.1 shows the required proximity for zone plates with outermost zone widths of 50 nm, 100 nm and 250 nm, for photon energies between 8

and 100 keV. For example, stacking two zone plates with an outermost zone width of 50 nm at a photon energy of 8 keV requires a proximity of 5.4 μm and a lateral alignment of 17 nm.

Experimental results for the increase of efficiency obtained from stacking two zone plates with an outermost zone width of 100 nm is shown in Fig. 2.12. We have developed a compact holder for stacking two such zone plates and use this system regularly in the 2-ID-E microprobe. Lateral alignment of the two zone plates is achieved by observing the Moire pattern from the two zone plates in real time and maximizing the fringe spacing by moving one of the zone plates. The zone plate stack is stable to within better than one zone width for the full duration of a 5-6 day run.

To quantify the proximity condition p , we have performed dynamical calculations of wave propagation through two stacked zone plates using coupled wave theory. Two identical gold zone plates with an outermost zone width of 100 nm were considered. A photon energy of 8 keV was chosen. A plane wave was assumed to impinge on the first zone plate. Both zone plates were assumed to be laterally aligned. The complex amplitudes of the electromagnetic field were calculated for the back side of the first zone plate, with a thickness of 1 μm , then used as input for propagation through the vacuum region of thickness t_2 , and the resulting amplitude used in turn used as input for calculation of the wave amplitudes at the rear side of the second zone plate. From the complex amplitudes, a total diffraction efficiency of the stack was calculated. Figure 2.13 shows results for a stack of two

Table 2.1. Proximity requirements for near-field stacking of zone plate lenses with three outermost zone widths for three hard x-ray energies.

dr_n [nm]	50			100			250		
energy [keV]	8	40	100	8	40	100	8	40	100
p [μm]	5.4	27	67	21	108	270	134	672	1680

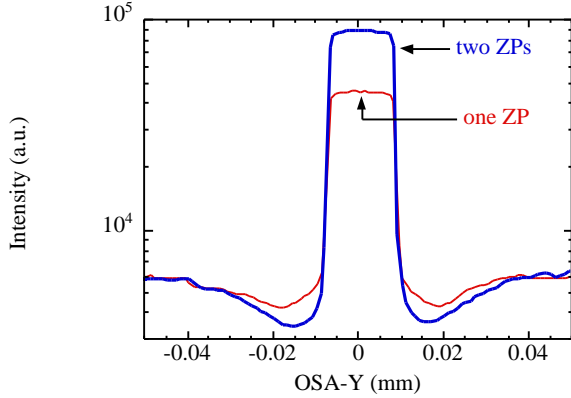


Fig. 2.12. Relative performance of one zone plate (ZP) vs. two stacked zone plates with outermost zone widths of 100 nm, at an energy of 8 keV.

zone plates with varying proximity parameter p .

2.3.3.2 Microfocusing with stacked zone plates

The focusing of x-rays to micron and even submicron dimensions has become routine at relatively low x-ray energies (< 20 keV) but is much more challenging at higher energies (40-100 keV). Motivated by possible applications, such as trace heavy-element detection by K-shell spectroscopy, fluorescence from dense materials, and bulk microdiffraction for stress measurements, an attempt to focus 50 keV undulator radiation using two closely juxtaposed zone plates

was carried out. The high-quality zone plates typically used for microfocusing are not thick enough to produce the desired phase shift at higher energies. The “stacking” of two zone plates effectively creates a thicker zone plate, but it is essential to control the placement of the zone plates to very high precision so that the outer zones will be in registry.

The microfocusing optics configuration is sketched in Fig. 2.14. In order for the two zone plates to behave as one, the second zone plate must be placed well within the near-field diffraction distance of the first, and their relative transverse positions must be adjusted to within a few hundred nanometers. The 50 keV undulator radiation incident on the zone plates was delivered by a Si (111) double-crystal monochromator. The two zone plates were separated by a few millimeters and located 60 m from the undulator source. This setup produced a focal spot of 9×7 microns with a focal distance of 1 m. The flux density gain was a factor of 24. Improvement of the performance should be possible by additional optimization of the zone-plate parameters.

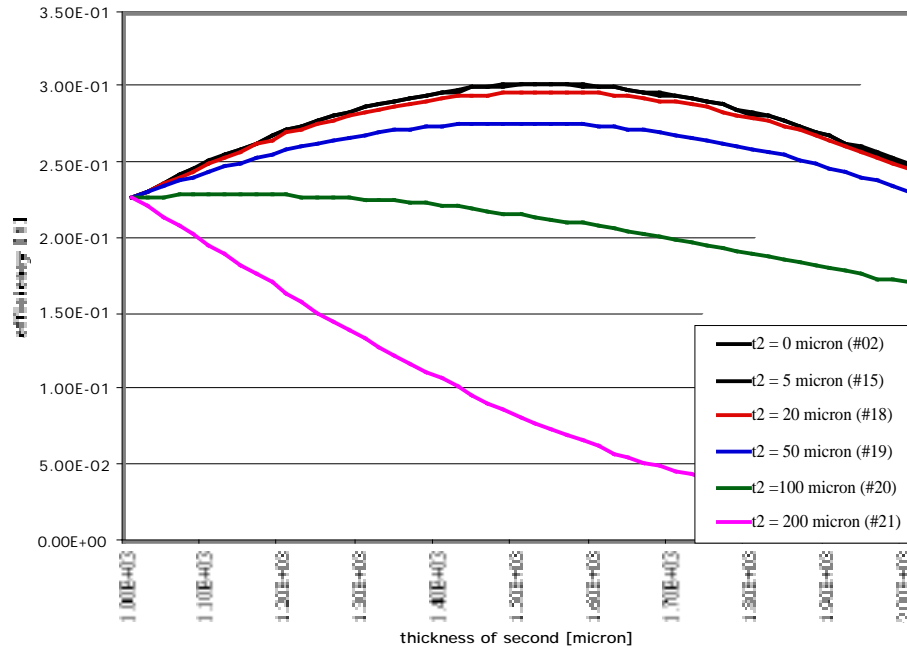


Fig. 2.13. Total efficiency of a stack of two zone plates with an outermost zone width of 100 nm, at a photon energy of 8 keV. The total efficiency of the stack is shown as function of the thickness of the second zone plate for different proximity parameter p . A fixed thickness of 1 μm was assumed for the first zone plate. Calculations for proximity parameters 0 μm , 5 μm , 20 μm , 50 μm , 100 μm and 200 μm are shown. Good agreement with the required proximity parameter of 20 nm, as derived from Fresnel diffraction, is demonstrated.

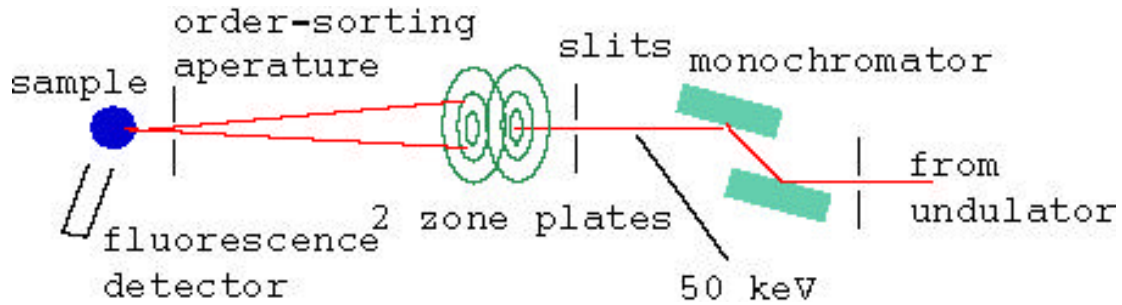


Fig. 2.14. Setup for stacked zone-plate experiment.

2.3.4 Imaging and Microfocusing Applications

2.3.4.1 Biological and medical applications

Two pathogenic mycobacteria, *Mycobacterium tuberculosis* and *Mycobacterium avium*, are intracellular pathogens that infect mainly mononuclear phagocytes and mucosal epithelial cells and survive within tissue macrophages. Tuberculosis is responsible for millions of deaths annually and one-fifth of all deaths of adults in developing countries. *M. avium* is the most common bacterial pathogen in AIDS patients managed in industrialized countries. The importance of macrophages for the survival and replication of both *M. tuberculosis* and *M. avium* in the host is widely appreciated, but little is known about the intracellular environment that permits intracellular survival and replication.

Once ingested by macrophages, *M. tuberculosis* and *M. avium* are present within membrane-bound inclusions that do not acidify or fuse with lysosomes. These phagosomes, although representing a stage of maturation between early and late phagosomes contain very similar host proteins as encountered in phagosomes that form around latex beads. Therefore, the reasons for the arrest of the vacuole maturation are unknown but are very likely due to the mycobacterial interference with the mammalian cell function. The intravacuolar localization of these mycobacteria suggests that they obtain sufficient nutrients required for intracellular multiplication, possibly by manipulating the macrophage to provide these nutrients.

Intracellular mycobacteria express a protein profile that is significantly different than that obtained when these organisms are cultured *in vitro*. It seems plausible that the expression of a number of these bacterial proteins is regulated by the conditions encountered within the vacuoles. These conditions would include the presence, absence, or actual concentration of particular elements like calcium, magnesium, iron, manganese, copper, potassium, and others that are important and necessary for the survival and replication of every organism.

We used the 2-ID-D hard x-ray microprobe to perform initial studies of the trace element distribution of metals in mycobacteria. By measuring and mapping the trace element distribution in the phagosome, we have taken first steps in investigating whether and how the concentration of particular elements might be related to the intracellular survival of pathogenic mycobacteria. This approach is supported by the fact that several cationic transporter genes have been found in the genomes of both *M. tuberculosis* and *M. avium*. By measuring the concentration of the particular elements in the phagosome infected by these pathogenic mycobacteria (*M. tuberculosis* and *M. avium*) and comparing it to the surrounding cytoplasm of the macrophage or to the concentration in phagosomes infected with an apathogenic mycobacterium (*M. smegmatis*) during the process of infection, we are gaining a first insight into the ability of pathogenic mycobacteria to acquire particular elements. By comparing differences in the ability to acquire particular elements in both pathogenic and apathogenic mycobacteria, we are also hoping to gain insight into how

this is related to the ability to cause disease. Due to the high elemental sensitivity and suboptical resolution of the microprobe and to the high penetration power of 10 keV x-rays, no other method method that we are aware of is capable of this type of study.

2.3.4.2 Environmental and geosciences

The microenvironment at and adjacent to actively metabolizing cell surfaces can be significantly different from the bulk environment. Cell surface polymers (lipopolysaccharides, extracellular polysaccharides), metabolic products, etc., can set up steep chemical gradients over very short distances. The behavior of contaminant radionuclides and metals in such microenvironments is currently difficult to predict because the chemistry of these environments has been difficult or impossible to define. The behavior of contaminants in such microenvironments can ultimately affect their macroscopic fates. Information about biogeochemical interactions at the microbe-geosurface microenvironment is paramount for predicting the fate of contaminants and effectively designing bioremediation approaches. State-of-the-art x-ray fluorescence (XRF) microimaging and spectro-microscopy are powerful techniques for resolving the distribution and speciation of contaminants on a microscopic scale. The objectives of our studies are (1) to determine the spatial distribution and chemical speciation of metals near bacteria-geosurface interfaces, and (2) to use this information to identify the interactions occurring near these interfaces among the metals, mineral surfaces, and bacterially

produced extracellular materials under a variety of conditions.

We have used hard x-ray phase zone plates to produce x-ray microbeams at the APS to investigate the spatial distribution of 3d elements in a single hydrated *Pseudomonas fluorescens* bacterium adhered to a Kapton film. The zone plate used in these microscopy experiments produced a focal spot size of 150 nm. The elements were mapped by scanning this sample in 150 nm steps through the focused monochromatic x-ray beam and integrating the selected K fluorescence intensity.

Figure 2.15 shows results of the x-ray microprobe measurements, qualitatively indicating the spatial distributions of K, Cr, Fe, Ni, Cu, and Zn in and near a hydrated *P. fluorescens* bacterium, adhered to a Kapton film at ambient temperature, that was exposed for 6 h to Cr 1000 ppm in solution. Observation of these images indicates that monitoring the spatial distribution of the K K fluorescence radiation coming from the sample enabled identification of the rod-shaped *P. fluorescens*, as well as the extracellular exudes associated with it. In addition, comparison of the distribution of Cr with that of K indicates that the majority of the Cr in this sample was associated extracellularly. Studies also have taken advantage of the ability to perform microspectroscopy experiments with the x-ray microbeam to create spatially resolved chemical speciation maps. These studies have identified the valence state of Cr adhered to the biofilm to be 3+, indicating a

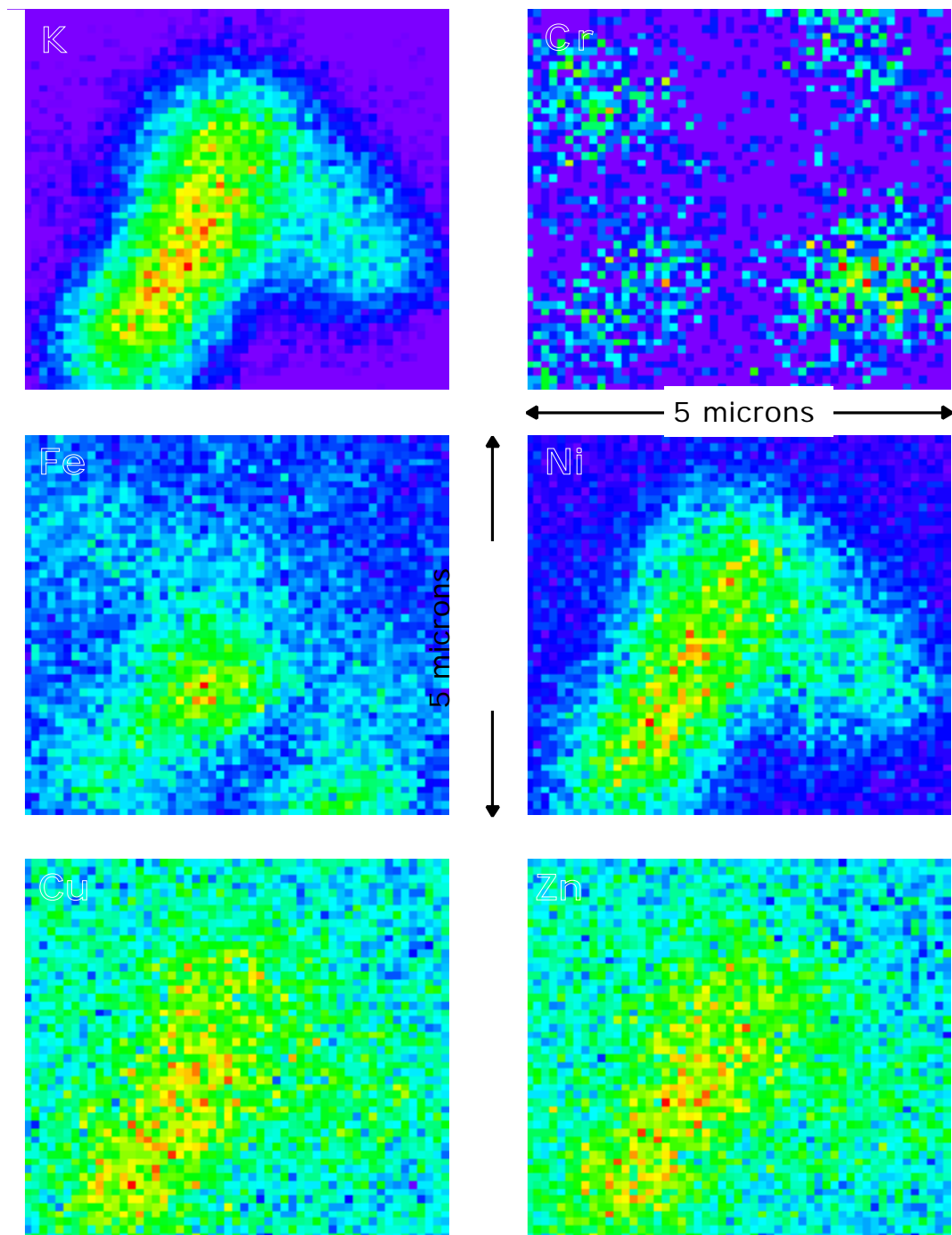


Fig. 2.15. Spatial distributions of K, Cr, Fe, Ni, Cu, and Zn in and near a hydrated *Pseudomonas fluorescens* bacterium, as measured by scanning x-ray fluorescence imaging.

reduction of the Cr from the 6+ state in which it was originally introduced. Recent studies have also demonstrated the ability of the XRF technique to spatially resolve the distribution of elements for single hydrated bacteria adhered to a thin-film mineral surface. The further development of these techniques for such applications promises to provide unique opportunities in the field of microbiology, geomicrobiology, and environmental research.

2.3.4.3 Nuclear materials studies

Zirconium alloys are extensively used in the nuclear industry as nuclear fuel cladding and structural fuel assembly components primarily because Zr is essentially transparent to neutrons. In nuclear reactors, one of the main degradation processes of Zr alloys, such as Zircaloy, is corrosion in high-temperature water. Corrosion and hydrogen ingress limit the useful lifetime of these alloys, and thus there is great economic incentive to minimize the amount of oxidation and hydriding that these materials experience in the reactor. The ability of Zircaloy to withstand corrosion and in-reactor degradation is impacted by its microstructure, in particular by the intermetallic precipitate size, morphology, and distribution and by the concentration of alloying elements in the Zr matrix. In addition, small changes in alloy chemistry, such as reduced tin content, have been implemented during the past decade to improve in-reactor corrosion performance.

A great amount of empirical knowledge exists correlating precipitate size, morphology and distribution (all of which depend on the thermomechanical treatment

as expressed by the annealing parameter) to corrosion performance, hydrogen pickup and in-reactor deformation. For instance, a surprising observation is the correlation of precipitate size on corrosion rate in pressurized water reactors (PWR) and boiling water reactors (BWR) reported by Garzarolli and Stehle (1986). In PWRs, large precipitates are desirable, as they decrease uniform corrosion rates. In BWRs, small precipitates are needed to decrease localized or nodular corrosion. In addition to the corrosion and hydrogen pickup varying with thermomechanical treatment for a given alloy, corrosion is also dependent upon alloy composition. Although relationships between microstructure and corrosion rates are understood empirically (i.e., the optimum annealing parameter to create a particular microstructure is well characterized), there is little mechanistic understanding of this process (Lemaignan and Motta, 1994).

In summary, we have empirical knowledge on the behavior of some alloys in both autoclave tests and in-reactor environments. This empirical knowledge relates corrosion behavior to heat treatment and therefore to the as-fabricated microstructure. It is thus important to characterize in detail the existing microstructure, in terms of precipitate structure and volume fraction, as well as the alloying content in the Zr matrix.

The second-phase precipitates are not detectable with standard bulk x-ray techniques, because their volume fraction in the alloy is on the order of 0.2 - 0.4%. These particles have traditionally been studied using transmission electron microscopy

(TEM), but, using TEM, it is difficult to obtain precise crystallographic information, as well as a true bulk picture of the types and quantities of second phases present after different heat treatments and irradiation schedules. The high brilliance and low background of the x-ray beams at the APS allowed us to determine the quantity and types of precipitates present in a material, by quickly acquiring enough diffraction information to estimate the phases present and their volume fraction in both unirradiated and neutron-irradiated samples.

The levels of alloying elements in the matrix are so low that they cannot be measured by traditional measurement techniques, such as energy-dispersive x-ray (EDX) analysis with TEM. There are chemical and spectroscopic techniques that can measure very low levels of alloying elements, in the bulk, but these are not suited to determining the alloying element content in specific regions in the microstructure. The unique combination of spatial and elemental resolution needed to measure to study the alloying elements in the hcp matrix of Zr alloys is available at the microbeamline at SRI CAT.

Answering these questions would have great technological benefit and would lead to the design of better cladding and more accurate predictions of corrosion in existing cladding, through more mechanistic and physically based corrosion models.

Microchemistry of the Zr alloy base metal

The solubility of transition metal alloying elements in the Zr matrix is very small (< 100 ppm) and cannot be detected with

traditional analysis techniques. This is because the techniques that have the spatial resolution to distinguish the matrix from the precipitates, such as TEM, do not have the elemental sensitivity to measure matrix concentrations below about 0.5% (5000 ppm). On the other hand, bulk techniques with higher compositional sensitivity do not have the spatial resolution to analyze only the Zr matrix. With the microbeam facility at the 2-ID-D/E beamline, we have the ideal combination of spatial and compositional sensitivity to measure these small concentrations of Fe and other transition elements in the matrix.

This facility was used to study the alloying content in the matrix of well-annealed Zircaloy 2 and Zircaloy 4, as well as the alloying element content of various standards including the above alloys in the quenched state, ultrapure zone-refined Zr. We examined TEM foils to avoid beam spreading resulting from the beam transversing the thickness of the sample. The results show very good agreement with the standards and allow the quantification of the alloying content of the matrix (Erwin et al., in press). To aid in this quantification, we have recently acquired a Monte Carlo program that can simulate the x-ray fluorescence process and can predict the results of the experiments.

Precipitate volume fraction as a function of thermal processing

We have used the 2-BM beamline to examine the precipitation kinetics of second phases in Zr alloys and to relate specific thermomechanical fabrication routes to a *quantitative* measure of second-phase particles present in the alloy in unirradiated

samples. This is, to our knowledge, the first time that such low levels of second phases in an alloy were detected in a bulk diffraction experiment.

Experiments on this beamline last year and earlier this year, indicated that the APS was capable of identifying by bulk diffraction analysis very small amounts of second-phase particles in Zr alloys (volume fraction $\sim 0.2\%$). We have examined ZIRLO, Zircaloy 2 and Zircaloy 4, identified the precipitate peaks as corresponding to the appropriate phases, and showed that their evolution could be followed with diffraction measurements in the APS (Delaire et al., in press). This research data has helped resolve other outstanding questions, such as which intermetallic phases are present in advanced alloys, such as ZIRLO.

To quantify the precipitate volume fraction, we are using Rietveld refinement, with the GSAS program, from Los Alamos National Laboratory. To that end we need a fairly complete data set for the 2-theta region of interest, as well as measurements performed on well-defined standards. We examined a series of samples with varying annealing parameters, either isochronally (different temperatures, fixed time of 1 h) or isothermally (different times, fixed temperature of 700°C), and are currently performing the Rietveld analysis. This research is being prepared for submission to the *Journal of Nuclear Materials*.

2.3.4.4 Nanotomography of chips

Over the last two years, we have seen an improvement in both spatial resolution and overall image quality in the tomography of

integrated circuit components at beamline 2-ID-B. In collaboration primarily with a research group at the National Institute of Standards and Technology, we have been developing tomographic imaging techniques capable of resolving submicron-sized structures, hence the term *nanotomography*. Our goal is to perform non-invasive imaging of buried integrated circuit constructions on the tens of nanometer length scale. These structures are not only excellent references for general nanoscale imaging development, they are also driving the development of a much-needed inspection tool for next-generation devices having defects on the order of 20 nm or smaller.

Our samples were taken from a test suite of electromigration-voided samples having a critical dimension of 0.35 μm for the transistor level and consisting of a two-level aluminum metallization stack (Ti/Al/Ti/TiN) joined by a tungsten via. An electromigration sample was prepared by maintaining a 2.3 mA current and a temperature of 220°C for 300 h, conditions that are typical of accelerated life testing. Although a void was formed in the interconnect, it still had electrical continuity because the Ti or TiN barrier layers or both were still intact. The samples were prepared for standard TEM measurements, meaning that the interconnect junctions with the W vias were in free-standing SiO₂ membranes $\sim 10 \mu\text{m}$ thick.

We employed scanning transmission x-ray microscopy to collect 2D projections of the samples over a range of angular orientations to the beam. The 2-ID-B scanning transmission x-ray microscope (STXM) utilizes coherent soft x-ray radiation from a

5.5 cm undulator after monochromatization by a spherical grating monochromator (McNulty et al., 1998). The STXM uses either an Au or a Ni zone plate having 100 nm or 45 nm finest zone widths, producing a near-diffraction-limited transverse resolution of 150 or 60 nm, respectively. The preliminary work was performed with both the 100 nm zone plate due to its higher diffraction efficiency, and the 45 nm zone plate was used in subsequent work for its better spatial resolution. We chose optimum photon energies in the region spanned by the Al and Si 1s absorption edges at 1559 and 1839 eV, respectively.

On a typical experimental run, we were able to acquire 12-14 projections evenly spaced over an angular range of $\pm 70^\circ$. This angular increment was initially limited by the rotational stage; the range was limited by the working distance between the sample and an order-sorting aperture pinhole, as well as by decreasing sample transmission at larger angles of incidence.

Tomographic reconstructions of these limited data sets involve solutions to underdetermined systems of equations. Different algorithms have been developed that work better or worse depending on the nature of the measured data set, e.g., in terms of signal to noise and number of projections. Also, one method may be preferable given certain *a priori* information about the sample. One aim of our work is to optimize the reconstruction quality, while at the same time trying to work with as reduced a set of projections as possible. These conditions will be common in upcoming high-throughput measurements in production-line environments.

Figure 2.16(a) shows the first results from STXM data acquired with the 100 nm zone plate (Levine et al., 1999). This reconstruction employed the simultaneous iterative reconstruction technique (SIRT). Two density isosurfaces are shown, green for medium and red for high (\sim twice medium) density. Tungsten is known to be present in the higher density via region. Surprisingly, similar densities were also observed in the centers of the two focused ion beam (FIB) markers, which are primarily aluminum with a TiN liner.

A comparison between the acquired and the reconstructed data for the normal incidence plane gives an indication of the uncertainties of the reconstruction method. These are seen to be about 400 nm, compared to an aluminum linewidth of 1.1 μm . Most of the small line artifacts can be ignored, but where they cross one of the FIB markers they increase its distortion. The set of angles sampled is much less than the Nyquist sampling limit, $1/2$ times the number of horizontal samples, or 394 in this case. Our number of projections is at least an order of magnitude less. As a consequence, there is no possibility that the 3D resolution will be as fine as the 2D resolution.

A Bayesian reconstruction algorithm was applied to the same projection data used to produce Fig. 2.16(a) (Levine et al., 2000). A view is presented in Fig. 2.16(b). No additional preprocessing was done. The image is much smoother than the SIRT reconstruction and more in accord with the acquired normal incidence projection in Fig. 2.16(c), which shows straight edges. The roughness present in the SIRT

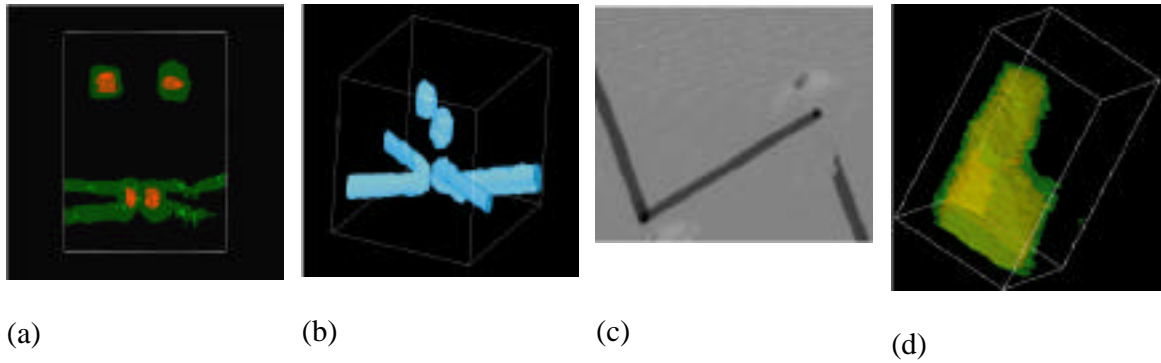


Fig. 2.16. (a) SIRT reconstruction of the integrated circuit with the ordinate y and the abscissa z . The two levels of interconnect are connected by vias. The two FIB markers are at the top of the image. This in-plane side view in practice cannot be observed directly in transmission. (b) Bayesian reconstruction of an integrated circuit interconnect using same data as in (a). The distance from the plane of the FIBs to the center of the upper interconnect line is $5.4 \pm 0.5 \mu\text{m}$. (c) Normal incidence projection of an integrated circuit interconnect with an electromigration void, imaged with 301×301 pixels with 57 nm step size and the 100 nm zone plate. The total field of view is $17.1 \mu\text{m}$. The dark marks at the intersection of aluminum metallization are the tungsten vias, which join two different levels. The light regions near the vias are the remnants of focused ion beam markers which fell out during sample preparation. (d) Bayesian reconstruction of the ragged end of the aluminum interconnect shown in the right side in (c).

reconstruction was used to estimate its spatial resolution at 400 nm . Here, an estimate is made based on the distance for a change in value by a factor of 0.735 when an abrupt change is expected. This is found to be 3.6 ± 1.0 pixel. Given a pixel size of $57 \pm 5 \text{ nm}$, the measured resolution in the 3D Bayesian reconstructed data is $200 \pm 70 \text{ nm}$, i.e., about twice as good.

Similarly, the Bayesian method was applied to a projection set acquired using the 45 nm zone plate from a circuit with an electromigration void. We failed to obtain a reconstruction with the Bayesian method for coarsely scanned data using the 100 nm zone plate, despite a successful SIRT reconstruction. For fine resolution data, Bayesian reconstructions were obtained without further preprocessing. The region of

the wire end is shown in Fig. 2.16(d). The resolution is estimated as above to be 7 ± 1 pixel, or $140 \pm 30 \text{ nm}$. This is comparable to a resolution of 10 ± 3 pixel or $200 \pm 70 \text{ nm}$ for SIRT. The uncertainty in the resolution is higher for SIRT because the isosurfaces generated by SIRT are rougher than those by the Bayesian method. The relative resolution of the two methods is 0.7 ± 0.2 and is independent of the pixel size and its uncertainty.

2.3.4.5 Noninterferometric quantitative x-ray phase imaging

Until recently, absorption was the principal contrast mechanism in transmission x-ray imaging and x-ray tomography experiments. As in medical applications, this leads to the ability to observe the projected density distribution in the object. However, imaging

based on absorption contrast can subject the specimen under study to a significant radiation dose leading to possible structural changes. This is particularly the case for x-ray imaging of biological structures at submicrometer resolution, where the imparted radiation dose can exceed 10^6 Gy in order to obtain high-quality images.

Consequently there has been considerable interest in the development of phase-contrast x-ray microscopy, especially under conditions where the absorption may be relatively low. This work is of interest in both full-field or direct-imaging microscopy and in soft x-ray holography. Moreover, away from absorption edges in the specimen, the phase-contrast mechanism becomes increasingly dominant at higher photon energies (absorption contrast decreases roughly as the third power of the photon energy, while phase contrast decreases linearly with it). For very energetic x-rays, objects may exhibit negligible absorption contrast yet show substantial phase contrast. In parallel, the importance of phase-contrast mechanisms has been accentuated by the availability of third-generation x-ray sources. These devices, by virtue of their high brilliance, have enabled phase-contrast imaging to become a simple and standard imaging technique. Phase-contrast tomography, while not yet commonplace, is also developing rapidly.

Early x-ray phase imaging arose from scanning transmission electron microscopy techniques and utilized quadrant detectors for phase analysis. Quadrant detectors have since been used in scanning transmission x-ray microscopy, and a similar technique has

been used in visible light microscopy. An advantage of this method is its spatial resolution, which is governed by the focal spot size of the scanning apparatus. The disadvantage is the time required to acquire a high-resolution image. Alternatively, whole image detection, for example with Shack-Hartmann arrays, is instrumentally complex and provides only limited spatial phase resolution. Whole image phase analysis in x-ray microscopy was also considered using Wigner deconvolution techniques. This is computationally intensive as it requires four-dimensional data sets. Multiple defocusing methods have also been developed, and various other iterative algorithms have appeared that successively approximate the phase by numerically propagating the complex amplitude between spatially separated planes. These techniques often intermix phase with absorption contrast or pose additional difficulties separating them. We tested a new method for x-ray phase determination that is neither computationally intensive nor depends upon complex x-ray optical schemes. This deterministic technique, which makes use of the derivative of the intensity over two or more longitudinally separated observation planes to retrieve the phase of the wave, utilizes the transport of intensity approach developed by Paganin and Nugent (1998). Its appeal is that it directly (noniteratively) retrieves spatially accurate, quantitative phase via an efficient numerical algorithm and uses standard x-ray microscopy techniques. We used it to explore the ability to extract the phase quantitatively from the absorption contrast, with a variety of samples ranging from essentially pure-absorption to pure-phase objects (Allman et al., 2000).

The experiments were performed with 1.83 keV x-rays at beamline 2-ID-B using two experimental configurations. The first was a holographic geometry (Fig. 2.17) in which test objects were illuminated from the diverging point source formed by the focus of a Fresnel zone plate lens. Holograms formed by interference between the waves scattered by the object and those that passed through unscattered were detected by a CCD camera. The second was a full-field imaging geometry (Fig. 2.18) in which points in the test object were directly imaged onto the CCD camera by the zone plate, functioning as an objective lens. The CCD camera in both cases used a thinned, backside-illuminated 1024 x 1024 pixel chip with 24- μm -square pixels and liquid nitrogen cooling, operated in direct x-ray detection mode. The spatial resolution obtained with the holographic geometry, ~ 60 nm, approached the diffraction limit of the zone plate that was used. The resolution obtained with the imaging geometry was limited to ~ 150 nm by the x-ray beam flight path (1 m) and CCD pixel size.

Figures 2.19 - 2.22 show intensity images and the retrieved phase images of various test objects obtained with both geometries. Of note is that the spider web segment in Fig. 2.22, a nearly pure phase object, showed significant phase but negligible absorption contrast. Overall, the measured phase obtained from the images obtained holographically agrees with the geometrically estimated phase to within $\pm 7\%$. That obtained with the imaging method agrees within $\pm 10\%$. In both cases the accuracy of the phase measurement was limited by the detected pixel resolution and precision to which the geometrical parameters were known.

These initial results indicate the promise of this technique for quantitative phase imaging of submicrometer structures. When fully developed, this method will help minimize the radiation dose and attendant artifact in high-resolution x-ray microscopy, as well as providing a valuable addition to the x-ray microscopist's toolbox.

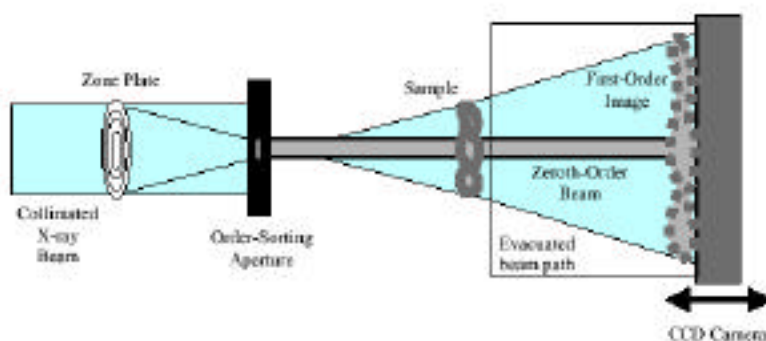


Fig. 2.17. Holographic geometry. The zone plate forms a near-diffraction-limited focal spot used to illuminate the sample. Coherent x-rays scattered by the sample interfere with those unscattered by it to form a hologram (first-order beam), which is recorded by the CCD camera. The zeroth-order beam from the zone plate is ignored.

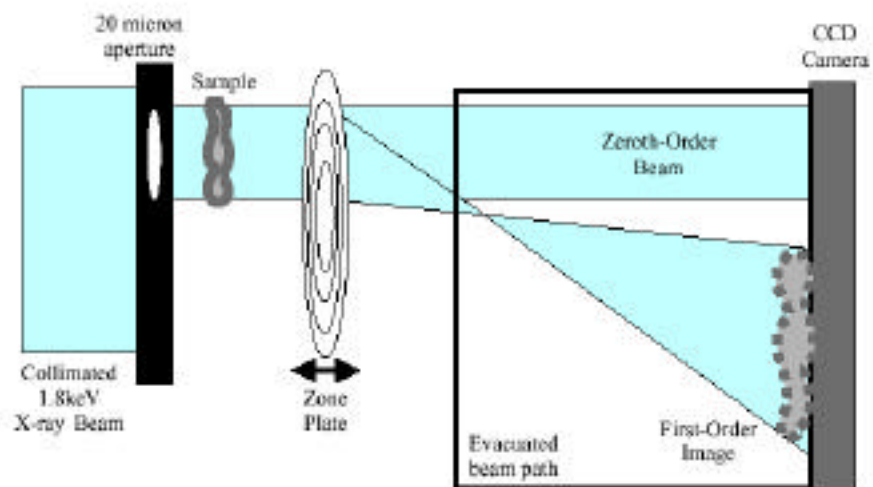


Fig. 2.18. Imaging geometry. The sample is illuminated by a coherent x-ray beam through a 20 μm pinhole. The zone plate incoherently images points in the sample onto the CCD camera (first-order image). The zeroth-order beam from the zone plate is ignored.

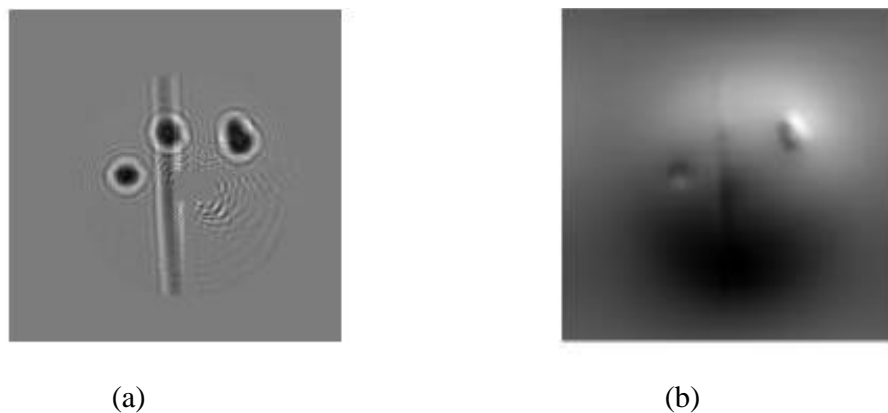
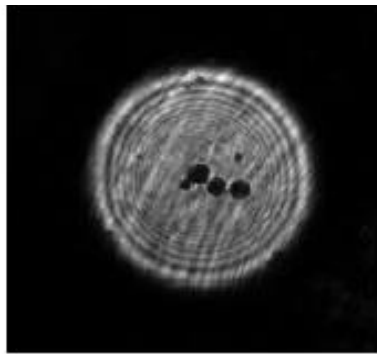
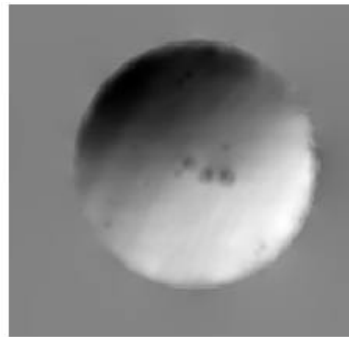


Fig. 2.19. Images of aluminum spheres (1-3 μm diameter) supported on a 100 nm formvar membrane, recorded with the holographic geometry. (a) Hologram intensity distribution after white-field (sample removed) background correction. (b) Image of retrieved phase. Visible in both images is a vertical fold in the formvar that displays significant phase distortion but low absorption.

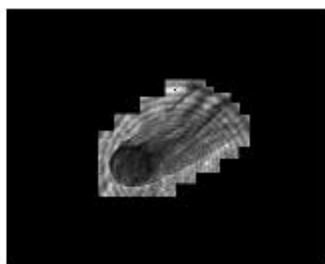


(a)

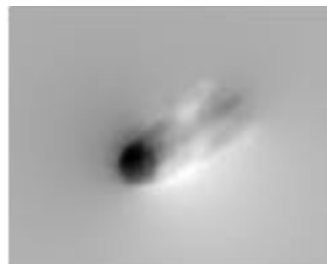


(b)

Fig. 2.20. Aluminum spheres recorded with the imaging geometry. (a) In-focus intensity distribution. (b) Retrieved phase.

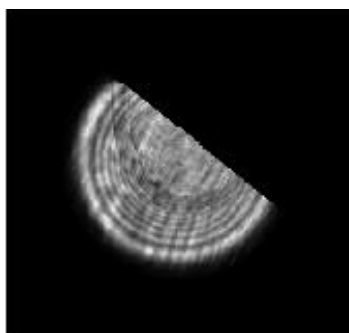


(a)



(b)

Fig. 2.21. A 3.7- μm -diameter plastic optical fiber, folded upon itself, recorded with the imaging geometry. (a) In-focus intensity distribution. Note that the absorption contrast of this predominantly phase object is weak. (b) Retrieved phase.



(a)



(b)

Fig. 2.22. A segment of spider web silk (1.8 μm diameter) recorded with the imaging geometry. (a) In-focus intensity distribution, showing barely detectable absorption contrast. This is essentially a pure phase object at 1.83 keV. (b) Retrieved phase.

2.3.4.6 Interferometry

The triple Laue (LLL) interferometer is one of the most widely used x-ray interferometers, be it in ultraprecise metrology (Chetwynd et al., 1998) or in imaging techniques (Momose, 1995). One feature of the LLL interferometer is that it can be used over a wide range of energies and is relatively easy to manufacture. As a first attempt into x-ray interferometry, we have built and tested (on 1-ID) a triple Laue interferometer (Fig. 2.23) achieving better than 90% fringe visibility.

An example of the imaging capability of the LLL is shown in Fig. 2.24. Figure 2.24(a) shows the interferogram obtained with a glass capillary [Fig.2.24(b)] placed in one of the LLL beam paths. The recorded fringes are for equal optical thickness and indicate the direction and modulus of the gradient. Since the thickness of the glass varies in a smooth and continuous fashion, this phase information would not be attainable with single-beam or in-line interferometric techniques.

The Laue transmission geometry has two significant problems: 1) absorption losses in each of the blades reduce intensity, and 2) Borrmann broadening in the last blade limits spatial resolution. An interferometer with all Bragg reflections has neither of these problems and has been proposed by Graeff and Bonse (1997). Their idea was to simultaneously excite the Si (440) and Si (404) reflections, creating split beams, and then to combine the branches after several Bragg reflections. Our version of this interferometer is shown in Fig. 2.25. This type of interferometer is dispersive and has a fixed operating energy with a narrow energy range (Fezzaa and Lee, 2000). Our interferometer was designed to have an operating energy of 7.46 keV.

Figure 2.26 shows the setup and results for a measurement where the intensity through a 50 μm aperture was monitored while sliding a 4° plastic wedge in one branch of the interferometer. A thin piece of plastic attenuator in the other arm compensates for the absorption loss through the wedge. The measured contrast was 93%.

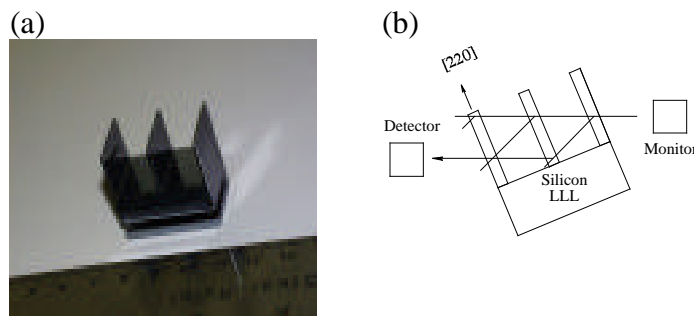


Fig. 2.23. The LLL interferometer (a) and a schematic of its operating mode (b).

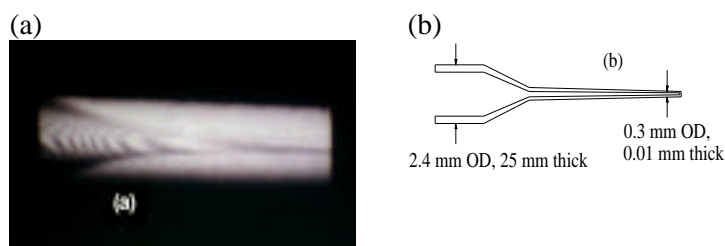


Fig. 2.24. An LLL interferogram of a glass capillary (a) and a schematic of the glass capillary (b).

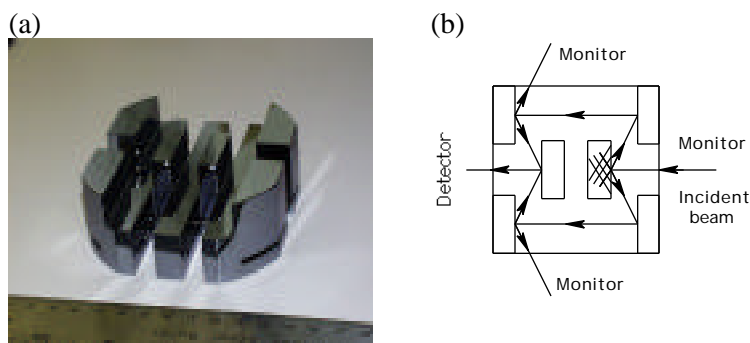


Fig. 2.25. Bragg reflection interferometer (a) and a schematic of its operating mode (b).

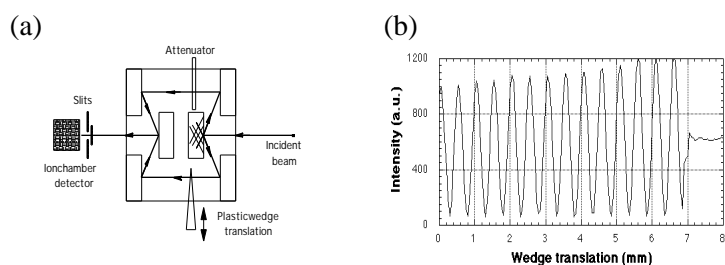


Fig. 2.26. Schematic of the Bragg reflection interferometer with a plastic wedge as a sample (a) and the resultant fringes (b).

We also tested this interferometer using 14.91 keV and the (880) and (808) reflections. Figure 2.27 shows the resultant Moiré pattern from an 8° plastic wedge that was inserted to cover half of one of the branches of the interferometer. The resulting effect of this linear phase gradient is a tilt of the fringes, which confirms that the Moiré

pattern is indeed a two-beam interference effect. No fringes were seen when one branch of the interferometer was blocked.

A modified version of the above interferometer with a variable optical path difference was fabricated by putting

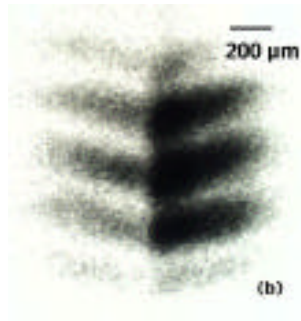


Fig. 2.27. An image of the fringes produced by putting a plastic wedge into the Bragg reflection interferometer operating at 14.91 keV.

a 1° angle into the faces in one of the arms of the interferometer. This angle allows a variation of the path length when the crystal is translated laterally. A wedge scan was made for each position, and the resulting fringes contrast was measured. Ideally, this interferometer would have no defocusing effect, and the fringe contrasts would only depend on the longitudinal beam coherence. However, due to fabrication imperfections, both longitudinal (ℓ_L) and transverse (ℓ_T) coherence lengths were involved. The data give $\ell_L = 50 \mu\text{m}$ and $\ell_T = 14 \mu\text{m}$ at 7.46 keV and $\ell_L = 350 \mu\text{m}$ and $\ell_T = 100 \mu\text{m}$ at 14.92 keV, which is within 10% of the calculated values. These coherence lengths are for the beam transmitted through the interferometer and not for the incident beam. The interferometer has a much smaller bandpass and angular acceptance than the incident beam. This smaller bandpass and angular acceptance are the determining factors for these coherence lengths.